Strain effects on the optical properties of lead-halide perovskites

Muscarella, Loreta Angela

[Link to publication in University of Groningen/UMCG research database](#)

2. EFFECTS OF GRAIN SIZE AND ORIENTATION ON OPTICAL PROPERTIES
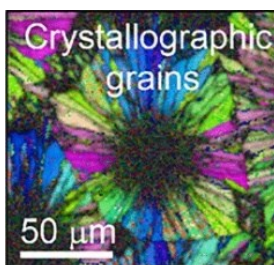
Growing large, oriented grains of perovskite often leads to efficient devices, but it is unclear if properties of the grains are responsible for the efficiency. Domains observed in SEM are commonly misidentified with crystallographic grains, but SEM images do not provide diffraction information. We study methylammonium lead iodide (MAPbI$_3$) films fabricated via flash-infrared annealing (FIRA) and the conventional antisolvent (AS) method by measuring grain size and orientation using electron back-scattered diffraction (EBSD) and studying how these affect optoelectronic properties such as local photoluminescence (PL), charge carrier lifetimes, and mobilities. We observe a local enhancement and shift of the PL emission at different regions of the FIRA clusters, but we observe no effect of crystal orientation on the optoelectronic properties. Additionally, despite substantial differences in grain size between the two systems, we find similar optoelectronic properties. These findings show that optoelectronic quality is not necessarily related to the orientation and size of crystalline domains.

2.1 Introduction

As discussed in **Chapter 1**, lead-halide perovskites have recently gathered significant attention due to the high efficiency of perovskite-based solar cells and other optoelectronic devices[1,2]. One of the most surprising properties of these materials is that the performance is very tolerant to different methods of fabrication[3–5], different compositions[6,7], and chemical treatments[8–10]. This robustness is reflected in high photoluminescence quantum efficiencies (PLQEs)[11,12], which is a measure of the fraction of radiative versus non-radiative decay, and therefore a direct measurement of the optical quality. In solar cells, the PLQE, for example, is directly related to the open-circuit voltage[13]. In practice, PLQE is reduced by the presence of defects[13,14] which are often related to chemical impurities such as interstitials, vacancies, dangling bonds[15,16] or defects on the surface and grain boundaries[17–19]. Both bulk and surface defects have been extensively studied in perovskites[20–23], and efficient passivation strategies are now routinely employed to achieve high LED and solar cell efficiencies[24–26]. In addition, chemical methods (*e.g.* Lewis bases[21] or chloride-based additives[6,27]) in the perovskite precursor are often applied to grow larger grains which has been thought to suppress non-radiative recombination pathways by reducing the number of grain boundaries[28–30]. Furthermore, these changes in the synthesis route affect the crystal growth and therefore the preferred crystallographic orientations[8,31,32].

However, it is unclear if the changes in grain size and orientation obtained by these treatments cause the improved optoelectronic properties, or if these are mainly related to passivation effects from the additives. Crystallographic orientation and their relation to the photoluminescence and other properties have not been studied in thin films so far because spatial resolution of the crystallographic parameters was lacking. Furthermore, the morphological "grain" observed in SEM images does not necessarily correspond to a crystallographic grain; so additional information is needed in order to relate the grain size with optoelectronic properties.

In this chapter, we use EBSD based on a direct-electron detection as described in **Chapter 1.5** to measure size, orientation, and rotation of

crystallographic grains in polycrystalline MAPbI₃ films with high spatial resolution. We study a MAPbI₃ thin film where crystallization is induced by FIRA, a low cost and rapid synthesis method[33,34]. These films exhibit large grains (tens of micrometers) highly oriented along the (112) and (400) planes in the direction parallel to the substrate. We find that the growth is spherulitic, *i.e.* starting from needle-like arrays, yielding ~100 micrometer sized clusters that consist of radially grown grains. With EBSD mapping we find two crystal orientations in the FIRA films that are well-separated in pairs in the large clusters of grains. We compare the PL from these clusters and find that PL intensity and spectrum is the same for the two crystal orientations. These results suggest that the two crystallographic orientations found do not govern the optical quality of perovskite thin films. Similarly, we find comparable emission in the interior part of the grain and at the grain boundaries (GBs) but we find enhanced emission and a red-shift at the cluster boundaries (CBs) and at the nucleation sites, which we attribute to favourable light-outcoupling and self-absorption. Finally, we compare the FIRA sample to one where crystallization is induced by the conventional AS dripping method, from the same precursor solution. This method produces sub-micron grains with random orientation. In our case, both samples show comparable charge carrier mobility and lifetime demonstrating that these properties are not necessarily determined by the grain size, at least for grains above a few hundred nanometers.

2.2. Fabrication-dependent Microstructure

To study the relation between the perovskite crystal orientation and its optoelectronic properties we first synthesize MAPbI₃ on ITO *via* FIRA wherein the spin-coated perovskite film is annealed using a short (1.2 second), highly intense infrared illumination to induce nucleation, as previously reported[33]. For comparison we also fabricate a sample by the AS method where chlorobenzene is rapidly poured onto the liquid precursor while spin coating. Both the FIRA and AS sample were fabricated from the same precursors under identical conditions, and thus the only difference is the crystallization process. Details on the fabrication are reported in the **Experimental Methods 2.5**. We probe the

morphology of both samples using scanning electron microscopy (SEM) as shown in **Figure 2.1a,b** and **Figure A2.1**. SEM images show a dramatic difference in cluster size from the AS method (100 nm - 2 µm) compared to FIRA (~100 µm). The differentiation between morphological grains (or clusters) observed in the SEM and real crystallographic grains is still largely misunderstood[35,36] and often, these clusters seen in SEM images are assigned to grains. In crystallography, the term "grain" is defined by a coherently diffracting domain of solid-state matter which has the same structure as a single crystal[37]. Therefore, from SEM images alone it is not possible to define the apparent domains as crystallographic grains because diffraction information is not measured. For this reason, we use "clusters" to describe the large perovskite domains shown in SEM images. We analyse the bulk crystal structure of the two systems deposited on ITO using X-ray diffraction (XRD). The AS sample shows a tetragonal XRD pattern where peaks from (110), (112), (220), (310) planes arise from the background[38,39].
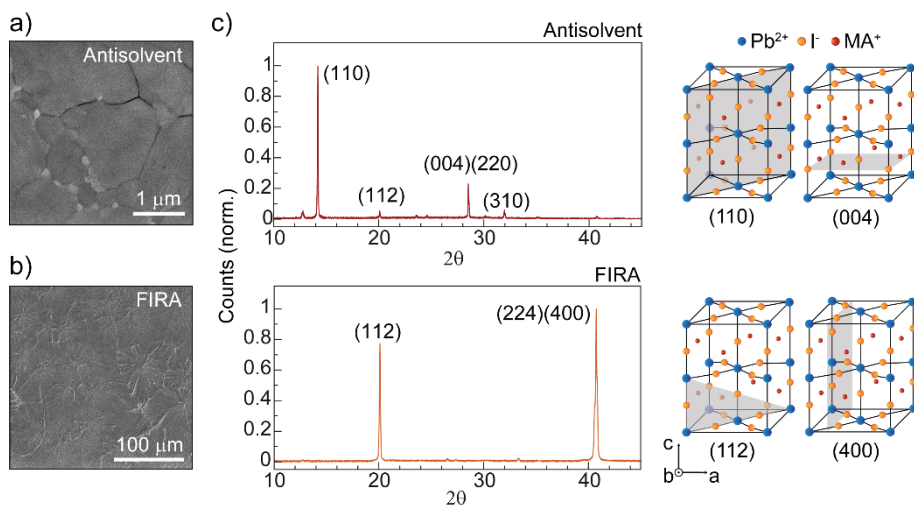

Figure 2.1. *Morphology and crystal orientation of AS and FIRA sample deposited on ITO.* SEM image of MAPbI₃ crystallized with **a)** AS and **b)** FIRA, **c)** XRD pattern of AS and FIRA MAPbI₃ with the corresponding unit cell cut along the (110) and (004) planes for the AS sample and along (112) and (400) for the FIRA sample.

In contrast, the FIRA sample shows a strong preferential orientation along the (112) and (400) planes (**Figure 2.1c**). A cut-off of the primitive tetragonal cell with the planes which show the highest diffraction peaks is shown next to the diffraction patterns. To investigate the crystal growth of the FIRA sample, we apply infrared annealing with varying pulse duration (**Figure 2.2a**). After 0.2 s of annealing, we observe a needle-like crystal morphology. After 0.5 s the crystals have grown in a space-filling manner by branching from the parental needle until each domain impinges with neighbouring domains resulting in straight boundaries. Optical microscopy of the final films (**Figure 2.2b**) shows large perovskite clusters in agreement with the SEM images.
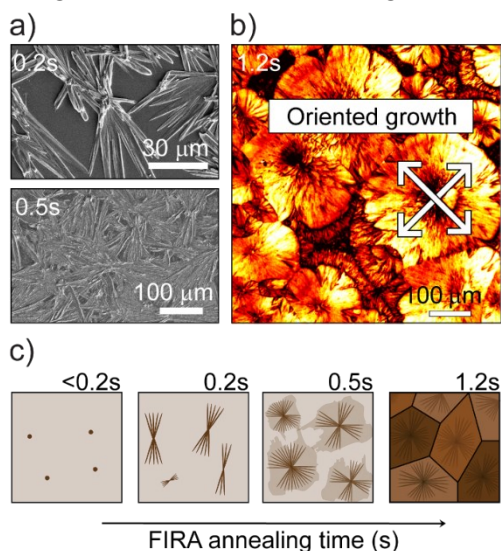
Figure 2.2. *Spherulitic growth mechanism of MAPbI₃ results in paired oriented domains.* **a)** SEM of FIRA film after 0.2s and 0.5s of infrared annealing, **b)** Polarized microscopy image of the final FIRA film showing paired oriented perovskite domains, **c)** Schematic spherulitic growth of perovskite films after 0.2, 0.5, 1, and 1.2 s of FIRA annealing.

We use polarized light microscopy to find how the two orientations observed in the XRD are spatially distributed. **Figure 2.2b** shows the presence of paired oriented domains within FIRA films for all the clusters (see also **Figure A2.2**) originated by the change in polarization of the incident polarized light caused by the two different refractive indices in the different crystal directions. This is a

indication of spherulitic growth (schematically shown in **Figure 2.2c**) *via* non-crystallographic branching[40] typical for many polymeric materials[41] and inorganic salts[42]. Interestingly, there also seems to be a common direction to all clusters, suggesting a global effect from temperature or strain gradient. In general, spherulitic growth requires the use of a saturated solution, high viscosity, and slow crystallization. This growth is also catalysed by the presence of impurities[40] or strain in the material. In this case, MAPbI$_3$ and the ITO (or quartz) show a substantial difference in the thermal expansion coefficient (α_{MAPbI3} =6.1 $\times$ 10^{-5} K^{-1}, α_{ITO} = 0.85 $\times$ 10^{-5} K^{-1}, α_{quartz} = 0.37 $\times$ 10^{-5} K^{-1} [43]), which has been shown to be the origin of strain during the cooling process after the thermal annealing[44]. Thus, strain can be considered as a factor inducing spherulitic growth in our system.

Recently, Adhyaksa et al.[48] have pioneered the application of EBSD for MAPbBr$_3$ using a direct electron detector which allows for low accelerating voltage of 5 kV instead of 30 kV, and low sample currents of pA instead of nA in conventional systems. We use the same detection system to collect the Kikuchi patterns from our MAPbI$_3$ films. The obtained Kikuchi patterns allow for the identification of grains, their size and shape and the boundaries between them. By fitting the patterns, we can identify crystal phase, grain orientation and rotation, as previously described in **Chapter 1.5**. Importantly, since with EBSD diffraction information is measured, we can distinguish clusters from grains and define the crystallographic grain size of MAPbI$_3$ fabricated via FIRA and AS. Furthermore, being a spatially resolved technique, it allows the direct comparison of a specific crystallographic orientation or a specific grain size with other spatially resolved optoelectronic techniques. **Figure 2.3b,c** shows an overlay of the image quality (*brightness*, IQ) with inverse pole figure (*color*, IPF) of the AS and FIRA system along the *z-axis* (parallel to the substrate). The IQ maps the sharpness of the Kikuchi lines obtained from the EBSD measurement which gives qualitative indications about the crystallinity of the material, topographic effects (*e.g.* roughness), strain of the microstructure and grain boundaries. The IPF map represents the crystal orientation obtained from fitting the Kikuchi patterns to each pixel of the image with respect to a reference axis. Along the *z-axis* (parallel to the substrate), the AS sample (**Figure 2.3b**) shows randomly oriented grains

of hundreds of nanometers. On the contrary, in the FIRA sample (**Figure 2.3c**), all grains are aligned along [100] and [112] direction (green and purple color) and the two orientations are paired in larger regions, in agreement with XRD and polarized microscopy measurements. The distribution of orientations for the two samples clearly shows the mostly random orientation for the AS sample, and the bipolar distribution of orientations for the FIRA sample (**Figure 2.3d**). Consistent with XRD (**Figure 2.1c**), we observe significant orientation along both the [100] and [112] direction, but locally the ratio can vary as shown for another FIRA cluster in **Figure A2.3**. Orientation maps along *x-* and *y-axis* (perpendicular to the substrate) show random grain orientations for the AS sample (see **Figure A2.4**) and highly oriented and paired grains for the FIRA sample (**Figure 2.3e,f**). Distribution plots of the crystallographic orientations along *x-* and *y-* are also shown in **Figure A2.5** clearly identifying the difference in the crystallization for the FIRA and AS systems along the *x-* and *y-axis*. In **Figure 2.3e,f**, grain boundaries within the FIRA cluster and the nucleation site are shown in dark gray (low IQ value). As previously discussed, this can be attributed to the roughness of the area, lower crystallinity but also due to the large step size used during the measurement in comparison with the grain size of that region. A grain, by definition, has the same orientation in all three directions. More than 90% of the grains we measure are smaller than 1 μm^2 for the AS sample, while the FIRA samples shows 83% of the grains having an area between 0-30 μm^2 as we report in **Figure A2.6**. While the FIRA grains are large, they are smaller than the size of the clusters shown in SEM **Figure 2.3g**).
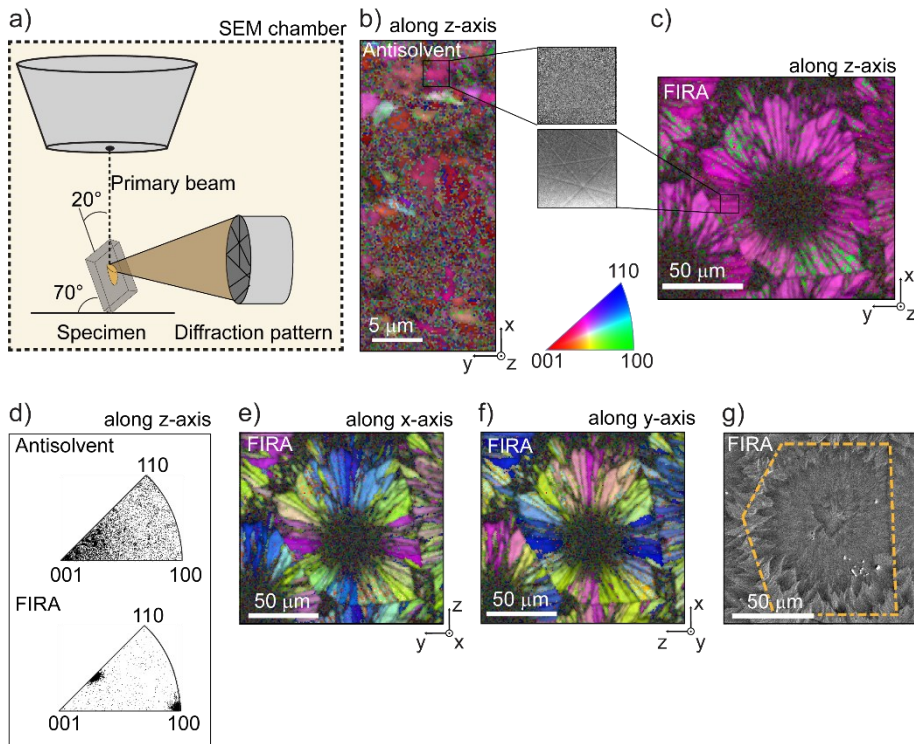
Figure 2.3. *EBSD maps reveal the crystal orientation and grain size of the two systems*. **a)** EBSD setup. **b)** IQ (brightness) overlay with IPF (color) map of AS sample showing crystallographic orientation along *z-axis*. Inset, a magnification of the typical Kikuchi patterns recorded from the sample. **c)** IQ (brightness) overlay with IPF (color) map of FIRA sample showing crystallographic orientation along *z-axis*. Inset, a magnification of the typical Kikuchi patterns recorded from the sample. **d)** Distribution of orientation for the two samples along z-axis. IQ (brightness) overlays with IPF (color) map of FIRA sample showing crystallographic orientation along **e)** *x*- and **f)** *y-axis*. **g)** SEM image showing the apparent grain size of a FIRA cluster. The cluster measured with EBSD is highlighted with a dashed line.

MAPbI$_3$ has an anisotropic tetragonal crystal structure and properties like trap-state density have been shown to be dependent upon crystal orientation[49,50]. In the following, we study the optoelectronic properties of the two well-characterized and spatially separated orientations shown by FIRA sample using

spatially resolved photoluminescence. Often, enlargement and preferential orientation of grains are achieved by introducing chemical additives which often also passivate the perovskite grains, prolonging lifetime and enhancing the photoluminescence. To avoid misleading attribution of the effects of additives to the grain size effects, here we compare the highly oriented FIRA and the AS samples fabricated without additives and from the same precursor solution.

2.3. Optoelectronic Properties

We measure the PL intensity using a confocal imaging microscope using 405nm laser as excitation source with a power density of 0.23 W/cm^2. As the two orientations on the sample are spatially well-separated, we can map any difference in PL emission between them. We measure a large area of the FIRA and AS samples including a whole FIRA cluster as shown in **Figure 2.4a** and **Figure A2.7** for a larger area. In the AS sample the PL intensity is relatively homogeneously distributed across the measured region, varying from cluster to cluster, consistent with many other works[51,52]. For the FIRA sample, we find comparable photoluminescence between the interior of the grain and the GBs. Previously grain boundaries were reported to cause either enhancement or reduction[29,48,53] of the emission intensity, mostly caused by ambiguities of assigning these boundaries. In our case, GBs do not lower the emission of the film. In contrast, the FIRA sample shows an enhancement in intensity of two to six-fold at the CBs and at the nucleation site where the spherulitic growth is started. To investigate the role of grain size on the PL intensity we compare the PL from the interior of the FIRA sample to the AS sample. In **Figure 2.4b** we plot PL spectra from five random regions of the two samples. Here we show that the interior region of the FIRA cluster shows a comparable PL intensity with the AS sample (FIRA Point 2&3), despite much larger size of the FIRA grains. This comparison shows that the PL emission is not solely determined by the grain size (at least for grains > 400 nm). Furthermore, we see no difference in wavelength or intensity for the regions that correspond to the two different, well-defined crystal orientations. Hence, the variation in PL emission intensity and wavelength are not related to the crystallographic orientations for the samples studied here.
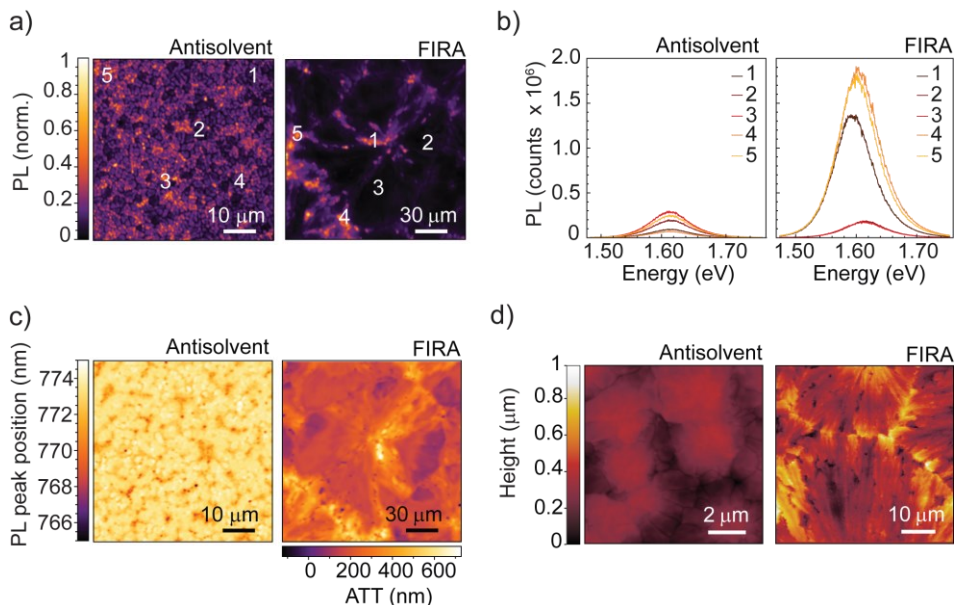
Figure 2.4. *Emission properties of MAPbI₃ varying crystal orientation and grain size.* **a)** Spatially resolved PL maps of AS and FIRA sample and corresponding **b)** PL spectra extracted from five random regions indicated in figure (a). **c)** Emission wavelength map of the same region as in figure (a) for the AS and FIRA samples. For the FIRA sample, the emission wavelength is converted into the additional travelled thickness ATT (on the horizontal scale bar) the light has been through before it is emitted and **d)** AFM image of AS and FIRA sample highlighting the CBs region in the FIRA sample.

The map of the PL peak position of the AS sample (**Figure 2.4c**) shows identical emission wavelength for every grain. In contrast, the FIRA sample shows a variation in emission wavelengths at distinct locations. The PL peak position at the CBs and nucleation point is red shifted compared to the interior of the cluster (**Figure 2.4c**). We also observe an asymmetric shape of the peak for the FIRA sample as shown in **Figure A2.8**. This shape, in combination with the red shift of the peak has been assigned to self-absorption when light travels through the perovskite layers before being emitted.[54] To validate this assignment we calculate the emission spectra expected from the light passing through different thicknesses of MAPbI₃ before being emitted. We calculate the red-shift

at the CBs and nucleation points we observe corresponds to light that has been travelling through 400nm – 800nm excess material as compared to the cluster interior region before being emitted (additional travelled thickness (ATT) on horizontal scale bar in **Figure 2.4c**). The calculation is reported in the **Appendix 2.6.2**. This is in good agreement with the observed thickness variation between the two regions in the AFM. From AFM measurements, the AS sample shows only minor height variation between the center and the rest of the grain (RMS roughness 70.5±7.5 nm, **Figure 2.4d**). On the contrary, the FIRA sample shows significant height variation at the CBs and at the nucleation point as shown in **Figure 2.4d** and in **Figure A2.9**. In these regions the film is around 400 nm to 1000 nm thicker compared to the interior of the cluster leading to a much larger roughness (RMS roughness is estimated 26.8±14.5 nm in the interior of the cluster, 175±47 nm at the nucleation site and 75.3±21 nm at the CBs).

The rough nature of the boundary observed in **Figure 2.4d** can favour light-outcoupling, as shown on patterned perovskite surfaces[55]. We hence tentatively assign the higher PL intensity in the CBs and nucleation site to better light-outcoupling at these rough surfaces. We corroborate the assignment of self-absorption and outcoupling differences by measuring PL lifetime maps of the FIRA sample. We observe a bi-exponential decay, with a fast and a slow component. The effect of reabsorption and photon recycling have been shown to affect the recombination dynamics by lengthening the slow lifetime component[55–58]. The lifetime of the FIRA sample at the CBs and at the nucleation site shows the same fast lifetime component, but a prolonged slow decay component compared to the interior of the cluster ($\tau_1 = 10.1 \pm 0.9$ and $\tau_2 = 49.2 \pm 2.0$ for the darker PL region in the grain interior and $\tau_1 = 12.9 \pm 0.9$ and $\tau_2 = 75.1 \pm 1.1$ for the brighter PL region at the CBs as reported in **Figure 2.5a,b**. The ratio of the slow-to-fast lifetime component (1.5 in our case) depends on the thickness and the likelihood of the light-outcoupling events[56]. The increased thickness increases the likelihood of re-absorption and increases the ratio, and better light-outcoupling decreases the lifetime ratio. Accounting only for difference in thickness at the CBs compared to the cluster interior, the lifetime ratio is overestimated. However, outcoupling is also most likely at rougher regions such as the CBs. Thus, the change in lifetime can be explained taking both the larger

thickness and outcoupling into account, consistent with the shift in PL spectrum. A semi-quantitative analysis is reported in **Appendix 2.6.3**. Similarly, no significant difference in lifetime is observed between the interior of the grain and the GBs within the FIRA cluster. We also do not observe a trend across the cluster that would correspond to the two different grain orientations. Thus, we do not find direct correlation between the crystal orientation and the PL intensity.
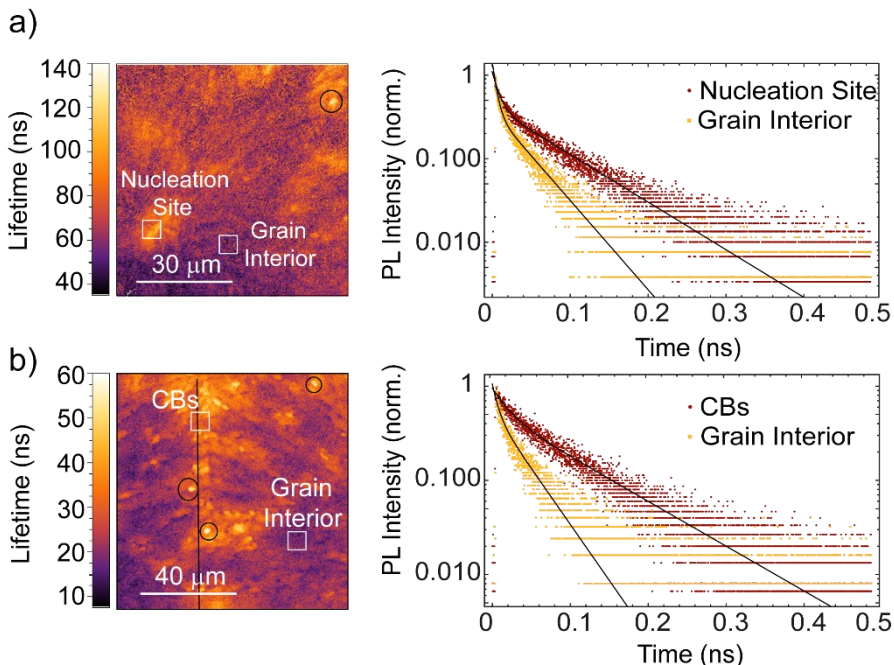

Figure 2.5. *Extended charge lifetime at the rough regions in the FIRA sample.* Lifetime maps of FIRA sample of the **a)** nucleation site and the **b)** CBs and corresponding decay curves of grain interior (darker) and CBs/nucleation site regions (brighter). Throughout the cluster the lifetime is comparable and neither shortening nor lengthening of lifetime is observed at the GBs within the FIRA cluster, while we observe longer slow component at the CBs and some long-lived hotspots. Lines represent the cluster boundaries and the long-lived hotspots are circled in black.

Next to the optical properties, the electronic properties have been shown to depend on grain size in some cases[59]. To investigate the mobility and recombination dynamics of photoexcited charge carriers in our two systems we

use the time-resolved microwave conductivity (TRMC) technique. The FIRA and AS samples were excited with 485 nm excitation wavelength. **Figure 2.6** shows the photoconductance ΔG as a function of time after pulsed excitation of AS and FIRA sample, respectively. The product of the yield of free charges φ and their mobility $\Sigma\mu$ (sum of electron and hole mobility) is derived from the maximum signal height (ΔG_{max}) which was divided by the fraction of absorbed photons for the two samples to take into account the difference in absorption.
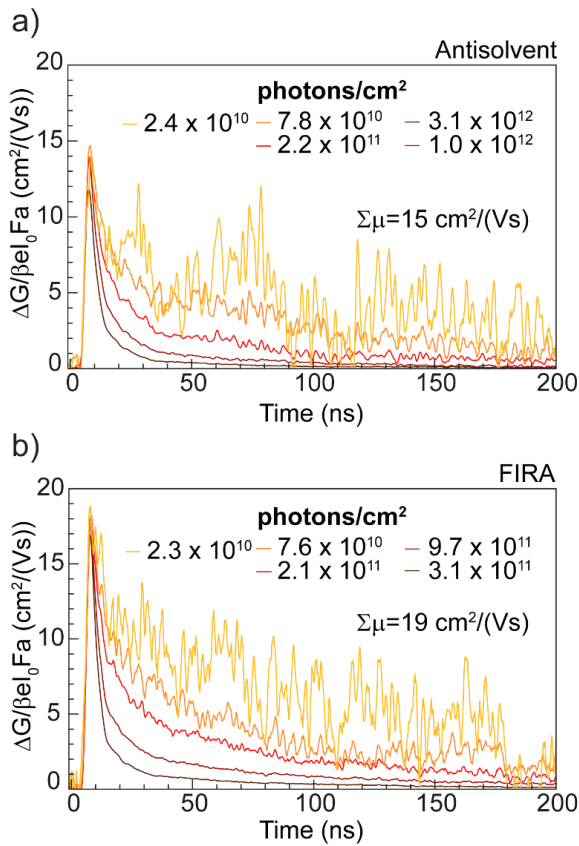

Figure 2.6. *Mobility and lifetime varying the grain size.* Time-resolved microwave conductivity (TRMC) traces measured at different carrier density for the **a)** AS and **b)** FIRA sample deposited on quartz.

We find a mobility of (15 ± 3) cm^2/(Vs) for the AS and (19 ± 4) cm^2/(Vs) for the FIRA sample, the difference of which is comparable to sample-to-sample

variation. The charge carrier lifetime is obtained from the photoconductance decay. The decay of the photoconductance represents the immobilization of free charges due to trapping or recombination. For both systems, we find that the lifetime of charges is in the order of a few hundred nanoseconds. We observe a slight increase of the effective mobility in the FIRA sample compared to the AS sample likely related to the enlarged grain size[59]. This difference is relatively small, despite the difference in grain size between the FIRA (tens of microns) and the AS sample (hundreds of nanometers). This shows that grain size alone does not dominate charge carrier transport properties. We note that the TRMC measurement mostly probes the local conductivity (~50 nm, more details about the probing length are reported in **Appendix 2.6.4**). Inter-grain transport across larger distances may show larger differences in crystallographically different systems. This finding is consistent with the similar device performances that have been reported for both FIRA and AS showing similar J_{sc}, V_{oc}, FF and PCE[33]. Practically, FIRA could allow a lower cost, environmentally friendly fabrication route to produce large scale, reproducible and more stable (**Figure A2.10**) perovskite compared to the AS method[33].

2.4. Conclusion

We have shown that the crystallographic orientation of $MAPbI_3$ grains does not determine the optical and local electronic properties. We study a $MAPbI_3$ thin film where crystallization is induced by FIRA. We apply EBSD to extract information about the microstructure of the perovskite thin film with high spatial resolution. The large FIRA clusters consist of grains that are tens of micrometer in size, highly oriented perpendicularly and in parallel to the substrate with a preferential orientation along the [112] and [100] direction along the *z-axis*. In comparison, a conventional sample fabricated via AS shows grains of hundreds of nanometers in size, randomly oriented in the three directions. We find increased PL intensity and a spectral shift in the FIRA sample at the CBs compared to the interior part of the FIRA cluster, which can be explained by roughness and thickness variations favoring light-outcoupling and self-absorption, respectively. No difference in PL between the grain and the GBs is

observed in the FIRA sample, leading us to the conclusion that in the grain boundaries are not detrimental to the PL in our system. Finally, we investigate charge carrier dynamics and find comparable lifetime and a slight increase in effective mobility in the FIRA and AS samples. We hence conclude that in our case, neither the grain size (when larger than a few hundred nm) nor the grain orientation are the dominant factor determining the optoelectronic properties of perovskite thin films. This finding implies that efforts towards a more efficient perovskite device may need to focus on reducing defects within the bulk and at the interface as well as impurities within the materials rather than growing large, oriented grains.

2.5. Experimental Methods

Sample Preparation

The precursor solution used to fabricate MAPbI$_3$ thin films is prepared at a concentration of 1M by mixing 1 M solutions of PbI$_2$ and MAI in a 1:1 ratio. The solutions are prepared in anhydrous 3 v/v DMF:1 v/v DMSO. For the AS film, the perovskite solution is spin-coated in two steps at 1000 and 6000 rpm for 10 and 20 s, respectively. During the second step, 100 µL of chlorobenzene is poured onto the substrate 5 s before the end of the spin coating program. Finally, the substrates are annealed at 100 °C for 1 h. The FIRA films are made by using the same precursor solution as described above. The spin-coating program consists of a single step at 4000 rpm for 10 s. Right after the spin coating, the substrates are irradiated with a 1.2 s short pulse of IR light to induce the crystallization of the perovskite.

X-Ray Diffraction

The X-Ray diffraction pattern of perovskite films deposited on ITO was measured using an X-ray diffractometer, Bruker D2 Phaser, with Cu Kα 1.5406 Å as X-Ray source, 0.002° (2θ) as step size, 0.150 s as exposure time. A FEI Verios 460 instrument was used to obtain SEM images. Atomic force microscopy (AFM) measurements were performed on a Veeco Dimension 3100 (Bruker) in tapping mode.

Optical Microscopy

Optical microscope (Zeiss, AxioCam ICc 5) equipped with a 10x/0.2 objective EC Epiplan, polarizer and analyzer set at different angles was used for polarized optical microscopy imaging. We combine the optical microscope in reflection mode with two polarizers, one placed in the light path before the specimen, and a second one, called analyzer, between the objective lenses and eyepieces.

Steady-State Photoluminescence

Steady-state PL of samples deposited on quartz was measured with a home-built setup equipped with a 640 nm continuous-wave laser as source of excitation (PicoQuant LDH-D-C-640) at a power output of 1 mW. Two Thorlabs filters, a long pass, ET655LP, and a notch, ZET642NF, were used to remove the excitation laser from the signal. The PL was coupled into a fiber connected to an OceanOptics USB4000 spectrometer. An integration time of 300 ms was used for each measurement.

Electron Back-Scattered Diffraction

The samples were prepared and kept in a nitrogen-filled glovebox to prevent degradation from moisture exposure before the measurement. Samples were deposited on ITO to avoid charging effects during the experiment. Samples were glued on a metallic stub with silver paste and left degassing for at least 2 hours in a humidity-controlled environment (<5%). Since the perovskite is a soft material, no additional mechanical treatments (e.g. mechanical polishing, grinding, electropolishing, ion milling) were applied before the measurement. The detector used is a direct electron detector based on the Timepix sensor from Amsterdam Scientific Instruments (ASI). The best parameters for the scans were found to be 15 keV as acceleration voltage, 100 pA as beam current, 100 ms as exposure time and working distances between 12 mm and 10.1 mm. This translates to the application of 10 nA per ms per pixel which is around 10^3 times lower compared conventional measurement reducing sample damage. The step size was chosen depending on the cluster size shown by the specific sample, 200 nm and 1 μm for the AS and FIRA sample, respectively. EBSD data were collected using EDAX OIM software and a Python script was used for image processing. The resulting Kikuchi patterns were indexed using tetragonal symmetry, $I4/mcm$, using 1-3° as degree of tolerance.

Spatially-resolved Photoluminescence

Spatially resolved PL maps were measured using a confocal imaging microscope (WITec alpha300 SR). A 405 nm laser diode (Thorlabs S1FC405) was used as excitation source where the PL intensity of the two MAPbI$_3$ films

was collected in reflection mode through a NA 0.9 objective using a spectrometer (UHTC 300 VIS, WITec) leading to a spatial resolution of 0.33 μm. The intensity was measured within the 700 to 840 nm emission wavelength range. A 488 nm LP filter was used to remove the excitation laser from the signal. The light collection was done from the same sample side as the excitation. The PL spectra were converted to the energy scale using a Jacobian transformation[60].

Time-Resolved Microwave Conductivity

Time-Resolved Microwave Conductivity (TRMC) was measured on AS and FIRA sample deposited on quartz. The thin films were placed in a sealed resonance cavity inside a nitrogen-filled glovebox to avoid degradation due to air exposure. The samples were excited at 485 nm using a pulsed excitation (10 Hz) and the photoconductance probed at different excitation densities. Neutral density filters were used to vary the intensity of the incident light. The ΔG signal rise is limited by the width of the laser pulse (3.5 ns FWHM) and the response time of the microwave system (18 ns). The slow repetition rate of the laser of 10 Hz ensures full relaxation of all photo-induced charges to the ground state before the next laser pulse hits the sample. The mobility $\sum \mu$ which is the sum of the electrons and holes mobility ($\mu_e + \mu_h$) is derived by the maximum signal height by the following equation[61],

$$\varphi \Sigma \mu = \frac{\Delta G_{max}}{\beta e I_0 F_A}$$ (2.1)

where I_0 is the number of photons per unit area per pulse, β a geometric factor related to the microwave cell, e is the elementary charge, φ is the charge carrier generation yield and F_A the fraction of the light absorbed by the sample at the excitation wavelength used. We assume φ to be unitary for the low exciton binding energy of the material.

Photoluminescence decay

Time-correlated single photon counting (TCSPC) measurements were performed with a home-built setup equipped with PicoQuant PDL 828 ''Sepia

II'' and a PicoQuant HydraHarp 400 multichannel picosecond event timer and TCSPC module. A 640 nm pulsed laser (PicoQuant LDH-D-C-640) with a repetition rate of 2 MHz was used to excite the sample. A Thorlabs FEL-700 long-pass filter was used to remove the excitation laser.

2.6. Appendix

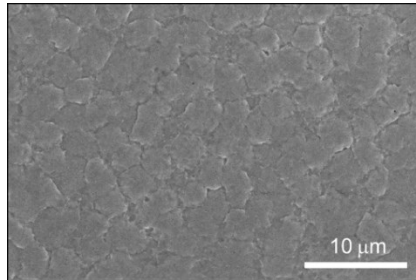### 2.6.1. ADDITIONAL FIGURES

Figure A2.1. SEM images of MAPbI$_3$ fabricated via antisolvent dripping at lower magnification. SEM shows perovskite domains of (sub-)micron size.
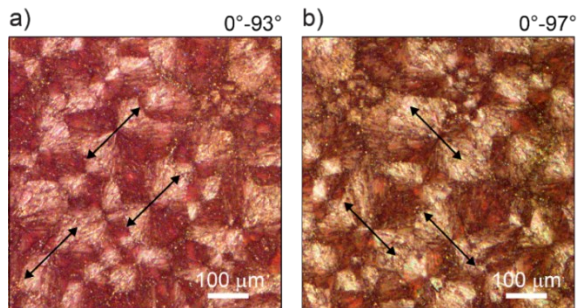

Figure A2.2. Polarized light microscopy of the same area of FIRA sample deposited on quartz. Analyser and polarizer are set at **a)** 0° and 93° and **b)** 0° and 97° degree, respectively. The perovskite shows a birefringent behaviour typical of spherulitic crystals.
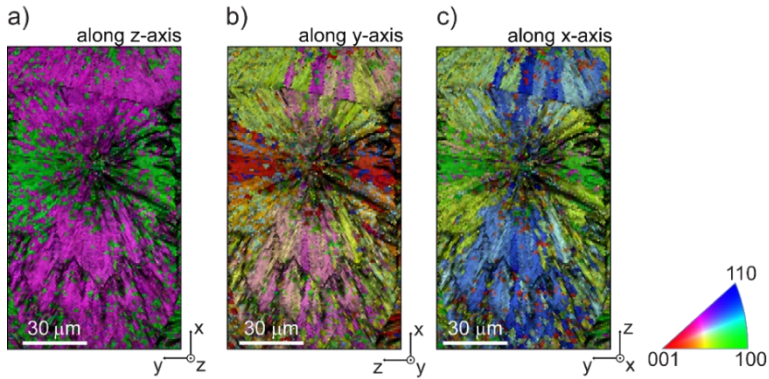
Figure A2.3. Image Quality (IQ) overlay with Inverse Pole Figure (IPF) map of the FIRA sample showing crystallographic orientation along **a)** z-direction, **b)** y-direction and **c)** x-direction. The perovskite domains that show homogeneous orientation along all three directions correspond to a crystallographic grain.
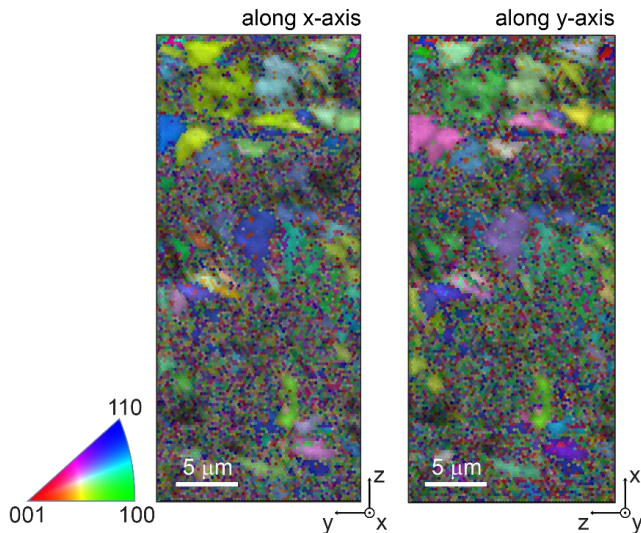

Figure A2.4. Image Quality (IQ, brightness) overlay with Inverse Pole Figure (IPF) map of AS sample showing crystallographic orientation along x-direction and y-direction. The perovskite domains that show homogeneous orientation along x-, y-, and z-direction correspond to a crystallographic grain.

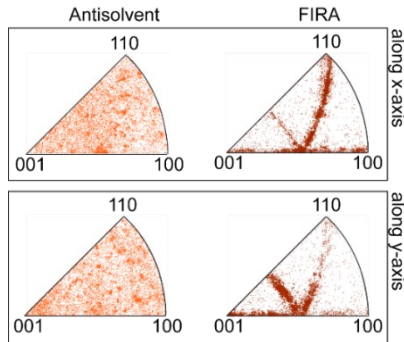**Figure A2.5.** Crystal orientation distribution along x-, y- and z-axis for AS and FIRA system. The AS system shows almost random orientation long the three directions while the FIRA system shows preferential orientation.
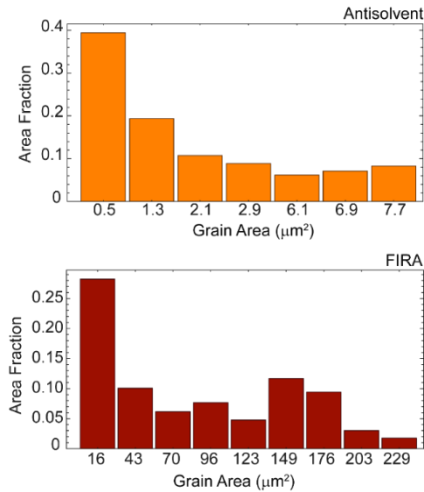
Figure A2.6. Grain area obtained from EBSD measurements in the AS and FIRA system. For the AS sample the binning in the histogram is 1 μm^2 and for the FIRA sample is 10 μm^2.
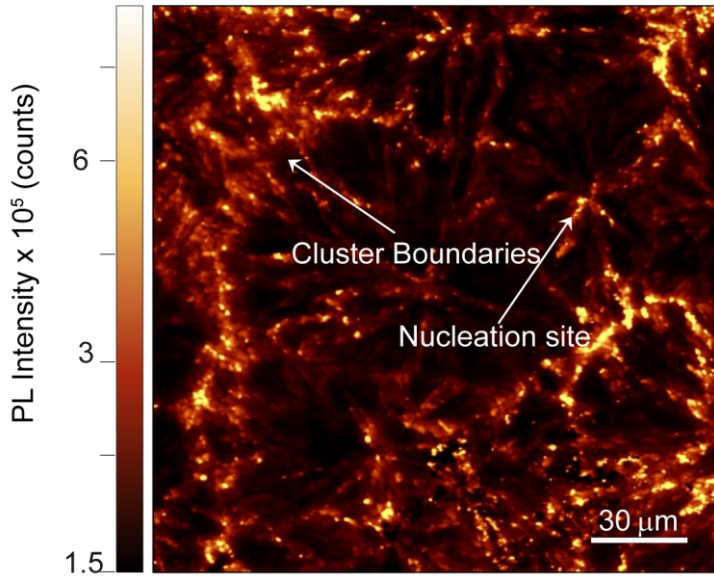
Figure A2.7. Spatially resolved PL of a bigger region of the FIRA sample including several clusters with a resolution of 0.33 μm per pixel. This map shows the enhancement in PL at the CBs and nucleation site for all the clusters. The enhancement varies from 4 to 6 times.
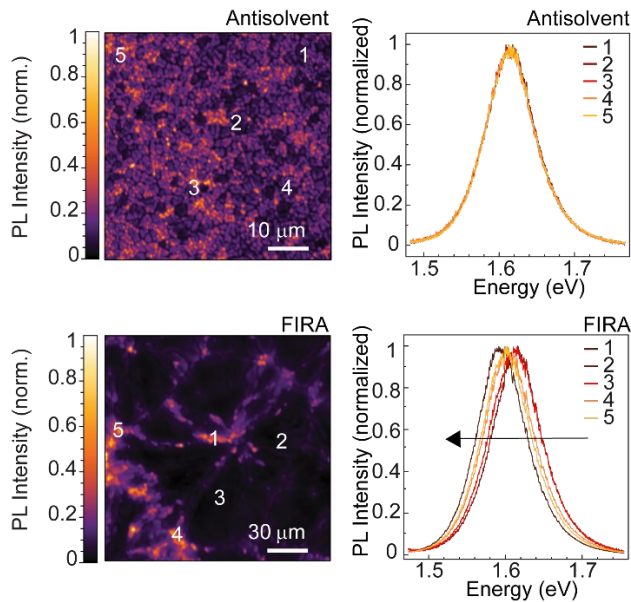
Figure A2.8. Normalized PL of the five regions highlighted in the main text for the AS and FIRA sample. The peak position in the AS sample remains constant in different regions showing no asymmetry in the emission peak, whereas in the FIRA sample the PL peak is red-shifted and more asymmetric moving from the interior region of the cluster (Point 2&3) to the CBs (Point 4&5) to the nucleation site (Point 1).
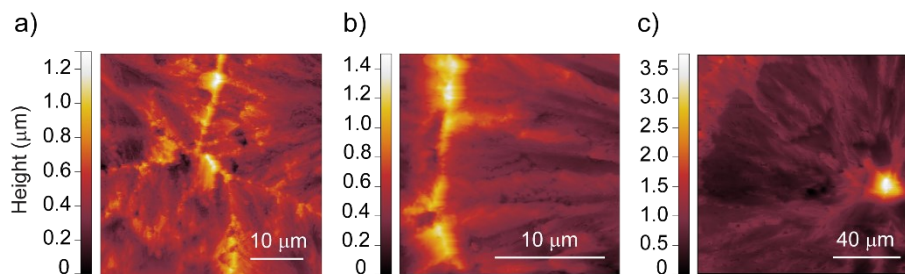
Figure A2.9. AFM images of FIRA sample at two different regions at a,b) the CBs and at c) the nucleation site
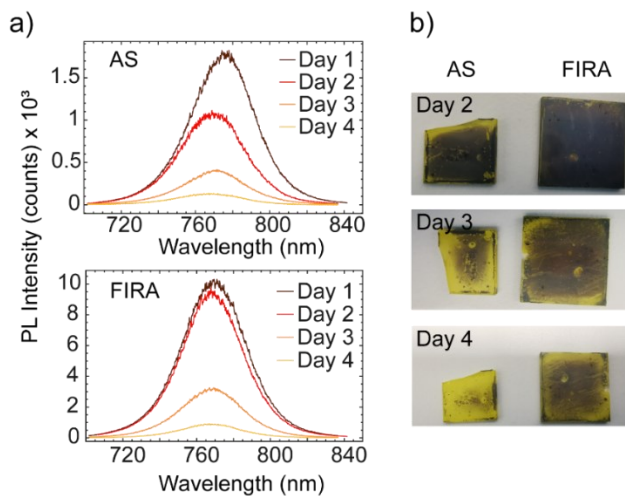
Figure A2.10. PL spectra of **a)** AS and FIRA measured after fabrication and up to 4 days of exposure to ambient conditions (with relative humidity of 22±4 RH% and temperature of 21±2 °C). **b)** Images of AS and FIRA films after 2, 3 and 4 days of air exposure.

2.6.2. ADDITIONAL THICKNESS TRAVELLED BY LIGHT

We simulate the expected PL spectra as a function of the additional travelled thickness (ATT) by the light before being emitted using the model following[54]

$$I_{emission}(d; \lambda) = I_{emission}(d_0; \lambda)e^{-\alpha(\lambda)d} \qquad (2.2)$$

where $I_{emission}(0; \lambda)$ is the PL spectrum of the interior region of the cluster used as reference, d is the thickness by which light is transmitted within the perovskite, $\alpha(\lambda)$ is the absorption coefficient obtained from absorption, $A(\lambda)$, as follows

$$\alpha(\lambda) = \frac{2.303\, A(\lambda)}{d_0} \qquad (2.3)$$

The model takes in account only the attenuation of the emitted light due to self-absorption events. In **Figure A2.11a**, we show the agreement of the simulated PL spectrum with the experimentally measured spectrum when the ATT is 250 nm. We convert the additional thickness transmitted by the light through the perovskite into the expected PL peak position using equation (2.1). Therefore, we fit a second order polynomial to find the relation between the PL peak position and the ATT (**Figure A2.11b**). Then the experimental emission wavelengths of the FIRA cluster shown in **Figure 2.4c** are converted using the relation obtained.
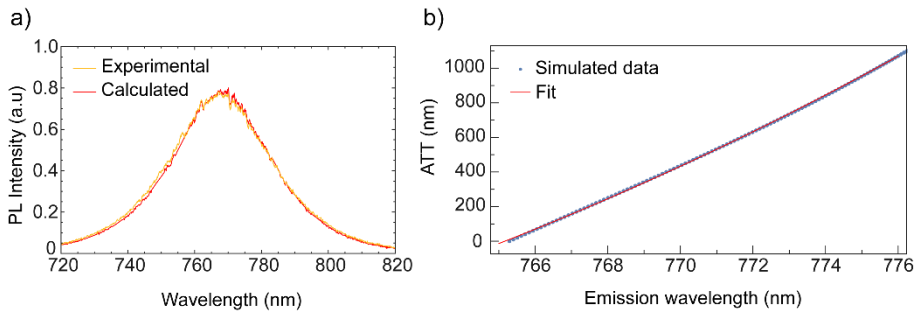
a)

b)

Figure A2.11. a) Experimental and simulated PL spectrum for additional transmitted thickness (ATT) of 250 nm. **b)** Relation between the PL peak position and the ATT before light being emitted

2.6.3. THICKNESS AND ROUGHNESS EFFECT ON LIFETIMES

The elongation of the radiative decay component due to photon recycling events has been observed in earlier works[55–57]. From Staub et al.,[56] the externally observed bimolecular component ratio is given by

$$k_{ratio}^{ext} = \frac{1 - p_{r,0}k}{1 - p_{r,CB}k}$$

(2.4)

Where k is the radiative fraction, $p_{r,0}$ and $p_{r,CB}$ is the probability for a photon to be reabsorbed in the layer before being emitted at the interior of the grain and at the cluster boundaries (CB), respectively. This term can be described as

$$p_r = 1 - p_e - p_p$$

(2.5)

and p_e is the probability for a photon to be emitted without reabsorption events which depends on the escape cone Ω, and p_p is parasitic absorption into the substrate. Assuming the radiative fraction k and p_p are constant, the radiative lifetime ratio at the grain interior and at the grain boundaries would only depend on the sample thickness and the escape cone

$$\frac{\tau_0}{\tau_{CB}} \approx \frac{1 - \left(\frac{p_{e,0}}{d_0} d\Omega_0 + \frac{p_{a,0}}{d_{CB}}\right)k}{1 - \left(\frac{p_{e,CB}}{d_{CB}} d\Omega_{CB} + \frac{p_{a,0}}{d_{CB}}\right)k}$$

(2.6)

where d_0 and d_{CB} are the thickness at the grain interior and at the cluster boundaries, respectively. $d\Omega_0$ and $d\Omega_{CB}$ are the escape cone at the grain and at the cluster boundaries. Experimentally we find the lifetime ratio to be 1.5. Accounting only for differences in thickness, the value obtained from calculation is 2.5, overestimating the one observed experimentally.

Light-outcoupling is favored by the difference in roughness of the surfaces. On average the grain interior and the cluster boundary regions show RMS roughness

of 26.8±14.5 nm and 75.3±21 nm, respectively. Thus, for the CBs, the $d\Omega_{CB}$ is increased and the lifetime ratio decreases in accordance with the experiments.

2.6.4. PROBING LENGTH IN TR-MICROWAVE CONDUCTIVITY

The distance crossed by the charges is limited by the charge carrier diffusion coefficient and half the oscillation period v (8.5 GHz), and the probing length P is given by:

$$P = \sqrt{\mu(k_B T/e)\frac{1}{2}v^{-1}} \tag{2.7}$$

Figure A2.12 shows the probing length at room temperature as function of mobility for different measurement frequencies.[4] If we now assume a 300 nm-sized grain in which the charges are homogeneously distributed, then ~83% of the charges will be generated within the TRMC probing length of 68 nm of a grain boundary. For a grain size of 10 μm, this would be less than 5%. Hence, the similar lifetimes of mobile charges for the different grain sizes means that the recombination is not significantly affected by the surface.
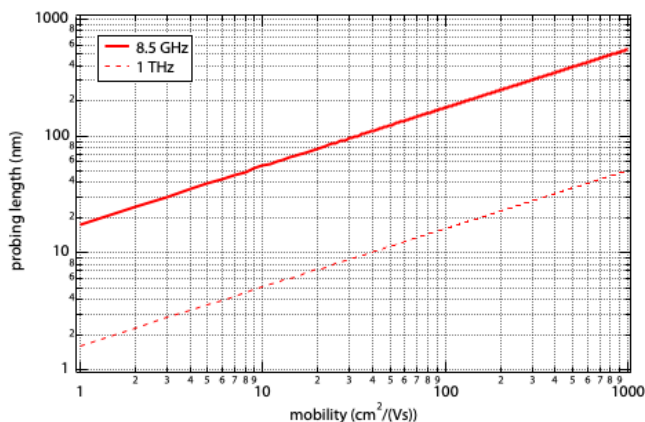

Figure A2.12. Probing length as function of mobility for photoconductivity measurements conducted at a frequency of 8.5 GHz (solid line, TRMC technique). This shows that the mobilities of 15 cm^2/(Vs) and 19 cm^2/(Vs) correspond to probing lengths of 68 nm and 76 nm, respectively. The probing length at 1 THz (dotted line, THz).

2.7. References

(1)   Chen, Y.; Zhang, L.; Zhang, Y.; Gao, H.; Yan, H. Large-Area Perovskite Solar Cells – a Review of Recent Progress and Issues. *RSC Adv.* **2018**, *8* (19). https://doi.org/10.1039/C8RA00384J.

(2)   Nie, W. Y.; Tsai, H. H.; Asadpour, R.; Blancon, J.-C. C.; Neukirch, A. J.; Gupta, G.; Crochet, J. J.; Chhowalla, M.; Tretiak, S.; Alam, M. A.; et al. High-Efficiency Solution-Processed Perovskite Solar Cells with Millimeter-Scale Grains. *Science* **2015**, *347* (6221). https://doi.org/10.1126/science.aaa0472.

(3)   Howard, I. A.; Abzieher, T.; Hossain, I. M.; Eggers, H.; Schackmar, F.; Ternes, S.; Richards, B. S.; Lemmer, U.; Paetzold, U. W. Coated and Printed Perovskites for Photovoltaic Applications. *Adv. Mater.* **2019**, *31* (26). https://doi.org/10.1002/adma.201806702.

(4)   Ren, Y.-K.; Shi, X.-Q.; Ding, X.-H.; Zhu, J.; Hayat, T.; Alsaedi, A.; Li, Z.-Q.; Xu, X.-X.; Yang, S.-F.; Dai, S.-Y. Facile Fabrication of Perovskite Layers with Large Grains through a Solvent Exchange Approach. *Inorg. Chem. Front.* **2018**, *5* (2). https://doi.org/10.1039/C7QI00685C.

(5)   Whitaker, J. B.; Kim, D. H.; Larson, B. W.; Zhang, F.; Berry, J. J.; van Hest, M. F. A. M.; Zhu, K. Scalable Slot-Die Coating of High Performance Perovskite Solar Cells. *Sustain. Energy Fuels* **2018**, *2* (11). https://doi.org/10.1039/C8SE00368H.

(6)   Jin, J.; Li, H.; Chen, C.; Zhang, B.; Xu, L.; Dong, B.; Song, H.; Dai, Q. Enhanced Performance of Perovskite Solar Cells with Zinc Chloride Additives. *ACS Appl. Mater. Interfaces* **2017**, *9* (49). https://doi.org/10.1021/acsami.7b15310.

(7)   Saliba, M. Polyelemental, Multicomponent Perovskite Semiconductor Libraries through Combinatorial Screening. *Adv. Energy Mater.* **2019**, *9* (25). https://doi.org/10.1002/aenm.201803754.

(8)   Huang, Y.; Wu, S.; Chen, R.; Fang, S.; Zhang, S.; Wang, G.; Chen, W. Efficient Methylamine-Containing Antisolvent Strategy to Fabricate High-Efficiency and Stable FA0.85Cs0.15Pb(Br0.15I2.85) Perovskite Solar Cells. *ACS Appl. Mater. Interfaces* **2019**, *11* (20). https://doi.org/10.1021/acsami.9b03323.

(9)   Klug, M. T.; Osherov, A.; Haghighirad, A. A.; Stranks, S. D.; Brown, P. R.; Bai, S.; Wang, J. T.-W.; Dang, X.; Bulovic, V.; Snaith, H. J.; et al. Tailoring Metal Halide Perovskites through Metal Substitution: Influence on Photovoltaic and Material Properties. *Energy Environ. Sci.* **2017**, *10* (1). https://doi.org/10.1039/C6EE03201J.

(10)   Mojtaba, A.; Ibrahim, D. M.; Aditya, S.; P., S. S.; Marius, F.; Neha, A.; Yuanyuan, H.; Khaja, N. M.; M., Z. S.; Michael, G.; et al. Impact of

Monovalent Cation Halide Additives on the Structural and Optoelectronic Properties of $CH_3NH_3PbI_3$ Perovskite. *Adv. Energy Mater.* **2016**, *6* (10). https://doi.org/10.1002/aenm.201502472.

(11) Abdi-Jalebi, M.; Andaji-Garmaroudi, Z.; Cacovich, S.; Stavrakas, C.; Philippe, B.; Richter, J. M.; Alsari, M.; Booker, E. P.; Hutter, E. M.; Pearson, A. J.; et al. Maximizing and Stabilizing Luminescence from Halide Perovskites with Potassium Passivation. *Nature* **2018**, *555* (497). https://doi.org/10.1038/nature25989.

(12) Halder, A.; Chulliyil, R.; Subbiah, A. S.; Khan, T.; Chattoraj, S.; Chowdhury, A.; Sarkar, S. K. Pseudohalide (SCN–)-Doped MAPbI3 Perovskites: A Few Surprises. *J. Phys. Chem. Lett.* **2015**, *6* (17). https://doi.org/10.1021/acs.jpclett.5b01327.

(13) Pazos-Outón, L. M.; Xiao, T. P.; Yablonovitch, E. Fundamental Efficiency Limit of Lead Iodide Perovskite Solar Cells. *J. Phys. Chem. Lett.* **2018**, *9* (7). https://doi.org/10.1021/acs.jpclett.7b03054.

(14) Sarritzu, V.; Sestu, N.; Marongiu, D.; Chang, X.; Masi, S.; Rizzo, A.; Colella, S.; Quochi, F.; Saba, M.; Mura, A.; et al. Optical Determination of Shockley-Read-Hall and Interface Recombination Currents in Hybrid Perovskites. *Sci. Rep.* **2017**, *7* (44629). https://doi.org/10.1038/srep44629.

(15) Meggiolaro, D.; De Angelis, F. First-Principles Modeling of Defects in Lead Halide Perovskites: Best Practices and Open Issues. *ACS Energy Lett.* **2018**, *3* (9). https://doi.org/10.1021/acsenergylett.8b01212.

(16) Ball, J. M.; Petrozza, A. Defects in Perovskite-Halides and Their Effects in Solar Cells. *Nat. Energy* **2016**, *1* (16149). https://doi.org/10.1038/nenergy.2016.149.

(17) Wang, J.; Fu, W.; Jariwala, S.; Sinha, I.; Jen, A. K.-Y.; Ginger, D. S. Reducing Surface Recombination Velocities at the Electrical Contacts Will Improve Perovskite Photovoltaics. *ACS Energy Lett.* **2019**, *4* (1),. https://doi.org/10.1021/acsenergylett.8b02058.

(18) Sherkar, T. S.; Momblona, C.; Gil-Escrig, L.; Ávila, J.; Sessolo, M.; Bolink, H. J.; Koster, L. J. A. Recombination in Perovskite Solar Cells: Significance of Grain Boundaries, Interface Traps, and Defect Ions. *ACS Energy Lett.* **2017**, *2* (5). https://doi.org/10.1021/acsenergylett.7b00236.

(19) Fassl, P.; Zakharko, Y.; Falk, L. M.; Goetz, K. P.; Paulus, F.; Taylor, A. D.; Zaumseil, J.; Vaynzof, Y. Effect of Density of Surface Defects on Photoluminescence Properties in MAPbI3 Perovskite Films. *J. Mater. Chem. C* **2019**, *7* (18). https://doi.org/10.1039/c8tc05998e.

(20) Uratani, H.; Yamashita, K. Charge Carrier Trapping at Surface Defects of Perovskite Solar Cell Absorbers: A First-Principles Study. *J. Phys. Chem. Lett.* **2017**, *8* (4). https://doi.org/10.1021/acs.jpclett.7b00055.

(21) Zhu, L.; Xu, Y.; Zhang, P.; Shi, J.; Zhao, Y.; Zhang, H.; Wu, J.; Luo, Y.; Li, D.; Meng, Q. Investigation on the Role of Lewis Bases in the Ripening Process of Perovskite Films for Highly Efficient Perovskite Solar Cells.

J. Mater. Chem. A **2017**, *5* (39). https://doi.org/10.1039/C7TA05378A.

(22) Stavrakas, C.; Zhumekenov, A. A.; Brenes, R.; Abdi-Jalebi, M.; Bulović, V.; Bakr, O. M.; Barnard, E. S.; Stranks, S. D. Probing Buried Recombination Pathways in Perovskite Structures Using 3D Photoluminescence Tomography. *Energy Environ. Sci.* **2018**, *11* (10). https://doi.org/10.1039/C8EE00928G.

(23) Staub, F.; Hempel, H.; Hebig, J.-C.; Mock, J.; Paetzold, U. W.; Rau, U.; Unold, T.; Kirchartz, T. Beyond Bulk Lifetimes: Insights into Lead Halide Perovskite Films from Time-Resolved Photoluminescence. *Phys. Rev. Appl.* **2016**, *6* (4). https://doi.org/10.1103/PhysRevApplied.6.044017.

(24) Lee, D. S.; Yun, J. S.; Kim, J.; Soufiani, A. M.; Chen, S.; Cho, Y.; Deng, X.; Seidel, J.; Lim, S.; Huang, S.; et al. Passivation of Grain Boundaries by Phenethylammonium in Formamidinium-Methylammonium Lead Halide Perovskite Solar Cells. *ACS Energy Lett.* **2018**, *3* (3). https://doi.org/10.1021/acsenergylett.8b00121.

(25) Zhang, H.; Wu, Y.; Shen, C.; Li, E.; Yan, C.; Zhang, W.; Tian, H.; Han, L.; Zhu, W. H. Efficient and Stable Chemical Passivation on Perovskite Surface via Bidentate Anchoring. *Adv. Energy Mater.* **2019**, *9* (13). https://doi.org/10.1002/aenm.201803573.

(26) Guo, Q.; Yuan, F.; Zhang, B.; Zhou, S.; Zhang, J.; Bai, Y.; Fan, L.; Hayat, T.; Alsaedi, A.; Tan, Z. Passivation of the Grain Boundaries of $CH_3NH_3PbI_3$ Using Carbon Quantum Dots for Highly Efficient Perovskite Solar Cells with Excellent Environmental Stability. *Nanoscale* **2019**, *11* (1). https://doi.org/10.1039/C8NR08295B.

(27) Zhang, W.; Saliba, M.; Moore, D. T.; Pathak, S. K.; Hörantner, M. T.; Stergiopoulos, T.; Stranks, S. D.; Eperon, G. E.; Alexander-Webber, J. A.; Abate, A.; et al. Ultrasmooth Organic–Inorganic Perovskite Thin-Film Formation and Crystallization for Efficient Planar Heterojunction Solar Cells. *Nat. Commun.* **2015**, *6* (6142). https://doi.org/10.1038/ncomms7142.

(28) Yang, Y.; Peng, H.; Liu, C.; Arain, Z.; Ding, Y.; Ma, S.; Liu, X.; Hayat, T.; Alsaedi, A.; Dai, S. Bi-Functional Additive Engineering for High-Performance Perovskite Solar Cells with Reduced Trap Density. *J. Mater. Chem. A* **2019**, *7* (11). https://doi.org/10.1039/C8TA11925B.

(29) Yang, M.; Zeng, Y.; Li, Z.; Kim, D. H.; Jiang, C.-S.; van de Lagemaat, J.; Zhu, K. Do Grain Boundaries Dominate Non-Radiative Recombination in $CH_3NH_3PbI_3$ Perovskite Thin Films? *Phys. Chem. Chem. Phys.* **2017**, *19* (7). https://doi.org/10.1039/C6CP08770A.

(30) Gedamu, D.; Asuo, I. M.; Benetti, D.; Basti, M.; Ka, I.; Cloutier, S. G.; Rosei, F.; Nechache, R. Solvent-Antisolvent Ambient Processed Large Grain Size Perovskite Thin Films for High-Performance Solar Cells. *Sci. Rep.* **2018**, *8* (1). https://doi.org/10.1038/s41598-018-31184-0.

(31) Foley, B. J.; Girard, J.; Sorenson, B. A.; Chen, A. Z.; Scott Niezgoda, J.;

Alpert, M. R.; Harper, A. F.; Smilgies, D.-M.; Clancy, P.; Saidi, W. A.; et al. Controlling Nucleation, Growth, and Orientation of Metal Halide Perovskite Thin Films with Rationally Selected Additives. *J. Mater. Chem. A* **2017**, *5* (1). https://doi.org/10.1039/C6TA07671H.

(32) Rong, Y.; Hou, X.; Hu, Y.; Mei, A.; Liu, L.; Wang, P.; Han, H. Synergy of Ammonium Chloride and Moisture on Perovskite Crystallization for Efficient Printable Mesoscopic Solar Cells. *Nat. Commun.* **2017**, *8* (14555). https://doi.org/10.1038/ncomms14555.

(33) Sanchez, S.; Hua, X.; Phung, N.; Steiner, U.; Abate, A. Flash Infrared Annealing for Antisolvent-Free Highly Efficient Perovskite Solar Cells. *Adv. Energy Mater.* **2018**, *8* (12). https://doi.org/10.1002/aenm.201702915.

(34) Sánchez, S.; Vallés-Pelarda, M.; Alberola-Borràs, J.-A.; Vidal, R.; Jerónimo-Rendón, J. J.; Saliba, M.; Boix, P. P.; Mora-Seró, I. Flash Infrared Annealing as a Cost-Effective and Low Environmental Impact Processing Method for Planar Perovskite Solar Cells. *Mater. Today* **2019,** *31*. https://doi.org/https://doi.org/10.1016/j.mattod.2019.04.021.

(35) Han, L.; Cong, S.; Yang, H.; Lou, Y.; Wang, H.; Huang, J.; Zhu, J.; Wu, Y.; Chen, Q.; Zhang, B.; et al. Environmental-Friendly Urea Additive Induced Large Perovskite Grains for High Performance Inverted Solar Cells. *Sol. RRL* **2018**, *2* (7). https://doi.org/10.1002/solr.201800054.

(36) Feng, J.; Zhu, X.; Yang, Z.; Zhang, X.; Niu, J.; Wang, Z.; Zuo, S.; Priya, S.; Liu, S. (Frank); Yang, D. Record Efficiency Stable Flexible Perovskite Solar Cell Using Effective Additive Assistant Strategy. *Adv. Mater.* **2018**, *30* (35). https://doi.org/10.1002/adma.201801418.

(37) Nalwa, H. S. *Handbook of Nanostructured Materials and Nanotechnology, Five-Volume Set*; Elsevier Science, **1999**.

(38) Zhou, Y.; Yang, M.; Vasiliev, A. L.; Garces, H. F.; Zhao, Y.; Wang, D.; Pang, S.; Zhu, K.; Padture, N. P. Growth Control of Compact CH$_3$NH$_3$PbI$_3$ Thin Films via Enhanced Solid-State Precursor Reaction for Efficient Planar Perovskite Solar Cells. *J. Mater. Chem. A* **2015**, *3* (17). https://doi.org/10.1039/C4TA07036D.

(39) Mali, S. S.; Hong, C. K.; Inamdar, A. I.; Im, H.; Shim, S. E. Efficient Planar N-i-p Type Heterojunction Flexible Perovskite Solar Cells with Sputtered TiO2 Electron Transporting Layers. *Nanoscale* **2017**, *9* (9). https://doi.org/10.1039/C6NR09032J.

(40) Shtukenberg, A. G.; Punin, Y. O.; Gunn, E.; Kahr, B. Spherulites. *Chem. Rev.* **2012**, *112* (3). https://doi.org/10.1021/cr200297f.

(41) Marentette, J. M.; Brown, G. R. Polymer Spherulites: I. Birefringence and Morphology. *J. Chem. Educ.* **1993**, *70* (6). https://doi.org/10.1021/ed070p435.

(42) Fu, W.; Vaughan, J.; Gillespie, A. Effects of Inorganic Anions on the Morphology of Sodium Oxalate Crystallized from Highly Alkaline

Solutions. *Cryst. Growth Des.* **2014**, *14* (4). https://doi.org/10.1021/cg5000952.

(43) Craciun, V.; Craciun, D.; Wang, X.; Anderson, T. J.; Singh, R. K. Transparent and Conducting Indium Tin Oxide Thin Films Grown by Pulsed Laser Deposition at Low Temperatures. *Thin Films Solid.* **2004**, *453*. https://doi.org/10.1016/j.tsf.2003.11.132.

(44) Zhao, J.; Deng, Y.; Wei, H.; Zheng, X.; Yu, Z.; Shao, Y.; Shield, J. E.; Huang, J. Strained Hybrid Perovskite Thin Films and Their Impact on the Intrinsic Stability of Perovskite Solar Cells. *Sci. Adv.* **2017**, *3* (11). https://doi.org/10.1126/sciadv.aao5616.

(45) Ryde, L. Application of EBSD to Analysis of Microstructures in Commercial Steels. *Mater. Sci. Technol.* **2006**, *22* (11). https://doi.org/10.1179/174328406X130948.

(46) Kamaya, M.; Quinta Da Fonseca, J.; Li, L. M.; Preuss, M. Local Plastic Strain Measurement by EBSD. *Applied Mechanics and Materials* **2007**, *7* (8). https://doi.org/10.4028/www.scientific.net/AMM.7-8.173.

(47) Rohrer, G. S.; Li, J.; Lee, S.; Rollett, A. D.; Groeber, M.; Uchic, M. D. Deriving Grain Boundary Character Distributions and Relative Grain Boundary Energies from Three-Dimensional EBSD Data. *Mater. Sci. Technol.* **2010**, *26* (6). https://doi.org/10.1179/026708309X12468927349370.

(48) Adhyaksa, G. W. P.; Brittman, S.; Āboliņš, H.; Lof, A.; Li, X.; Keelor, J. D.; Luo, Y.; Duevski, T.; Heeren, R. M. A.; Ellis, S. R.; et al. Understanding Detrimental and Beneficial Grain Boundary Effects in Halide Perovskites. *Adv. Mater.* **2018**, *30* (52). https://doi.org/10.1002/adma.201804792.

(49) Zhang, T.; Long, M.; Yan, K.; Zeng, X.; Zhou, F.; Chen, Z.; Wan, X.; Chen, K.; Liu, P.; Li, F.; et al. Facet-Dependent Property of Sequentially Deposited Perovskite Thin Films: Chemical Origin and Self-Annihilation. *ACS Appl. Mater. Interfaces* **2016**, *8* (47). https://doi.org/10.1021/acsami.6b11986.

(50) Leblebici, S. Y.; Leppert, L.; Li, Y.; Reyes-Lillo, S. E.; Wickenburg, S.; Wong, E.; Lee, J.; Melli, M.; Ziegler, D.; Angell, D. K.; et al. Facet-Dependent Photovoltaic Efficiency Variations in Single Grains of Hybrid Halide Perovskite. *Nat. Energy* **2016**, *1* (16093). https://doi.org/10.1038/nenergy.2016.93.

(51) Moerman, D.; Eperon, G. E.; Precht, J. T.; Ginger, D. S. Correlating Photoluminescence Heterogeneity with Local Electronic Properties in Methylammonium Lead Tribromide Perovskite Thin Films. *Chem. Mater.* **2017**, *29* (13). https://doi.org/10.1021/acs.chemmater.7b00235.

(52) de Quilettes, D. W.; Vorpahl, S. M.; Stranks, S. D.; Nagaoka, H.; Eperon, G. E.; Ziffer, M. E.; Snaith, H. J.; Ginger, D. S. Impact of Microstructure on Local Carrier Lifetime in Perovskite Solar Cells. *Science* **2015**, *348*

(6235). https://doi.org/10.1126/science.aaa5333.

(53) Castro-Méndez, A.-F.; Hidalgo, J.; Correa-Baena, J.-P. The Role of Grain Boundaries in Perovskite Solar Cells. *Adv. Energy Mater.* **2019**, *9* (38), 1901489. https://doi.org/10.1002/aenm.201901489.

(54) Mohan, V.; Jain, P. K. Spectral Heterogeneity of Hybrid Lead Halide Perovskites Demystified by Spatially Resolved Emission. *J. Phys. Chem. C* **2017**, *121* (35). https://doi.org/10.1021/acs.jpcc.7b08005.

(55) Richter, J. M.; Abdi-Jalebi, M.; Sadhanala, A.; Tabachnyk, M.; Rivett, J. P. H.; Pazos-Outón, L. M.; Gödel, K. C.; Price, M.; Deschler, F.; Friend, R. H. Enhancing Photoluminescence Yields in Lead Halide Perovskites by Photon Recycling and Light Out-Coupling. *Nat. Commun.* **2016**, *7* (13941). https://doi.org/10.1038/ncomms13941.

(56) Staub, F.; Kirchartz, T.; Bittkau, K.; Rau, U. Manipulating the Net Radiative Recombination Rate in Lead Halide Perovskite Films by Modification of Light Outcoupling. *J. Phys. Chem. Lett.* **2017**, *8* (20). https://doi.org/10.1021/acs.jpclett.7b02224.

(57) W. Crothers, T.; L. Milot, R.; B. Patel, J.; S. Parrott, E.; Schlipf, J.; Müller-Buschbaum, P.; B. Johnston, M.; M. Herz, L. Photon Reabsorption Masks Intrinsic Bimolecular Charge-Carrier Recombination in CH3NH3PbI3 Perovskite. *Nano Lett.* **2017**, *17* (9). https://doi.org/10.1021/acs.nanolett.7b02834.

(58) Diab, H.; Arnold, C.; Lédée, F.; Trippé-Allard, G.; Delport, G.; Vilar, C.; Bretenaker, F.; Barjon, J.; Lauret, J.-S. S.; Deleporte, E.; et al. Impact of Reabsorption on the Emission Spectra and Recombination Dynamics of Hybrid Perovskite Single Crystals. *J. Phys. Chem. Lett.* **2017**, *8* (13). https://doi.org/10.1021/acs.jpclett.7b00998.

(59) Reid, O. G.; Yang, M.; Kopidakis, N.; Zhu, K.; Rumbles, G. Grain-Size-Limited Mobility in Methylammonium Lead Iodide Perovskite Thin Films. *ACS Energy Lett.* **2016**, *1* (3). https://doi.org/10.1021/acsenergylett.6b00288.

(60) Mooney, J.; Kambhampati, P. Get the Basics Right: Jacobian Conversion of Wavelength and Energy Scales for Quantitative Analysis of Emission Spectra. *J. Phys. Chem. Lett.* **2013**, *4* (19). https://doi.org/10.1021/jz401508t.

(61) Savenije, T. J.; Ferguson, A. J.; Kopidakis, N.; Rumbles, G. Revealing the Dynamics of Charge Carriers in Polymer:Fullerene Blends Using Photoinduced Time-Resolved Microwave Conductivity. *J. Phys. Chem. C* **2013**, *117* (46). https://doi.org/10.1021/jp406706u.